Unraveling near-field origin of electromagnetic waves scattered from silver nanorod arrays using pseudo-spectral time-domain calculation

Bang-Yan Lin,[1] Hui-Chen Hsu,[2] Chun-Hao Teng,[3,*] Hung-Chun Chang,[1,4,5] Juen-Kai Wang,[2,6,§] and Yuh-Lin Wang[2,7]

[1]*Graduate Institute of Communication Engineering, National Taiwan University, Taipei, Taiwan, ROC*
[2]*Institute of Atomic and Molecular Sciences, Academia Sinica, Taipei, Taiwan, ROC*
[3]*Department of Mathematics, National Cheng Kung University, Tainan, Taiwan, ROC*
[4]*Department of Electrical Engineering, National Taiwan University, Taipei, Taiwan, ROC*
[5]*Graduate Institute of Photonics and Optoelectronics Engineering, National Taiwan University, Taipei, Taiwan, ROC*
[6]*Center for Condensed Matter Sciences, National Taiwan University, Taipei, Taiwan, ROC*
[7]*Department of Physics, National Taiwan University, Taipei, Taiwan, ROC*
[*]*Corresponding author: tengch@mail.ncku.edu.tw*
[§]*Corresponding author: jkwang@ntu.edu.tw*

Abstract: In this study, we report the investigation of both near- and far-field electromagnetic characteristics of two-dimensional silver nanorod arrays embedded in anodic aluminum oxide with the use of a high-accuracy three-dimensional Legendre pseudospectral time-domain scheme. The simulated far-field scattering spectra agree with the experimental observations. We show that enhanced electric field is created between adjacent nanorods and, most importantly, far-field scattered light wave is mainly contributed from surface magnetic field, instead of the surface enhanced electric field. The identified near-field to far-field connection produces an important implication in the development of efficient surface-enhanced Raman scattering substrates.

OCIS codes: (240.6680) Surface plasmon polariton; (240.6695) Surface-enhanced Raman scattering; (290.5850) Scattering: Particles

References and links

1. S. A. Maier and H. A. Atwater, "Plasmonics: Localization and guiding of electromagnetic energy in metal/dielectric structures," J. Appl. Phys. **98,** 011101-011110 (2005).
2. H. H. Wang, C. Y. Liu, S. B. Wu, N. W. Liu, C. Y. Peng, T. H. Chan, C. F. Hsu, J. K. Wang, and Y. L. Wang, "Highly Raman-enhancing substrates based on silver nanoparticle arrays with tunable sub-10 nm gaps," Adv. Mater. **18**, 491-495 (2006), and references therein.
3. T.-T. Liu, Y.-H. Lin, C.-S. Hung, T.-J. Liu, Y. Chen, Y.-C. Huang, T.-H. Tsai, H.-H. Wang, D.-W. Wang, J.-K. Wang, Y.-L. Wang, and C.-H. Lin, "A high speed detection platform based on surface-enhanced Raman scattering for monitoring antibiotic-induced chemical changes in bacteria cell wall," PloS One (in press).
4. S. Biring, H.-H. Wang, J.-K. Wang, and Y.-L.Wang, "Light scattering from 2D arrays of monodispersed Ag nanoparticles separated by tunable nano-gaps: spectral evolution and analytical analysis of plasmonic coupling," Opt. Express **16,** 15312-15324 (2008).
5. Y. C. Chang, J. Y. Chu, T. J. Wang, M. W. Lin, J. T. Yeh, and J.-K. Wang, "Fourier analysis of surface plasmon waves launched from single nanohole and nanohole arrays: unraveling tip-induced effects," Opt. Express **16**, 740-747 (2008).
6. J. Zhao, A. O. Pinchuk, J. M. McMahon, A. Li, L. K. Ausman, A. L. Atkinson, and G. C. Schatz, "Methods for describing the electromagnetic properties of silver and gold Nanoparticles," Acc. Chem. Res. **41**, 1710-1720 (2008).
7. B. T. Draine and P. J. Flatau, "Discrete-dipole approximation for scattering calculations," J. Opt. Soc. Am. A **11**, 1491-1499 (1994).
8. A. Taflove and S. C. Hagness, *Computational electrodynamics: the finite-difference time-domain method* (Artech House, Boston, 2005).

#110633 - $15.00 USD Received 27 Apr 2009; revised 7 Jul 2009; accepted 13 Jul 2009; published 31 Jul 2009

9. G. Mie, "Contributions to the optics of turbid media, especially colloidal metal solutions," Ann. Phys. **25**, 377-445, (1908).
10. K. S. Yee, "Numerical solution of initial boundary value problems involving Maxwell's equations in isotropic media," IEEE Trans. Antennas Propag. **14**, 302-307 (1966).
11. S. S. Zivanovic, K. S. Yee, and K. K. Mei, "A subgridding method for the time-domain finite-difference method to solve Maxwell's equations," IEEE Trans. Microwave Theory Tech. **39**, 471-479 (1991).
12. H. O. Kreiss and J. Oliger, "Comparison of accurate methods for the integration of hyperbolic equations. Tellus," **24**, 199-215 (1972).
13. T. Yamaguchi and T. Hinata, "Optical near-field analysis of spherical metals: application of the FDTD method combined with the ADE method," Opt. Express **15**, 11481-11491 (2007).
14. R. M. Stöckle, Y. D. Suh, V. Deckert, and R. Zenobi, "Nanoscale chemical analysis by tip-enhanced Raman spectroscopy," Chem. Phys. Lett. **318**, 131-136 (2000).
15. E. Fort and S. Grésillon, "Surface enhanced fluorescence," J. Phys. D **41**, 013001:1-31 (2008).
16. X. Ji, W. Cai, and P. Zhang, "High-order DGTD methods for dispersive Maxwell's equations and modelling of silver nanowire couping," Int. J. Numer. Meth. Engng. **69**, 308-325 (2007).
17. C.-H. Teng, B.-Y. Lin, H.-C. Chang, H.-C. Hsu, C.-N. Lin, and K.-A. Feng, "A Legendre Pseudospectral Penalty Scheme for Solving Time-Domain Maxwell's Equations," J. Sci. Comput. **36,** 351-390 (2008).
18. D. W. Lynch and W. R. Hunter, "Silver (Ag)" in *Handbook of optical constants of solids,* E. D. Palik, ed. (Academic Press, Orlando, 1985), pp. 350-357.
19. D. W. Thompson, "Optical characterization of porous alumina from vacuum ultraviolet to midinfrared," J. Appl. Phys. **97**, 113511:1-9 (2005).
20. J. L. Young and R. O. Nelson, "A summary and systematic analysis of FDTD algorithms for linearly dispersive media," IEEE Antennas Propag. Mag. **43,** 61-77 (2001).
21. M. H. Carpenter and C. A. Kennedy, "Fourth order 2N-storage Runge-Kutta scheme," NASA-TM-109112 (1994).
22. M. H. Carpenter and D. Gottlieb and S. Abarbanel, and W. S. Don, "The theoretical accuracy of Runge-Kutta time discretizations for the initial boundary value problem: A careful study of the boundary error," SIAM J. Sci. Comp. **16,** 1241-1252 (1995).
23. S. Abarbenel and D. Gottlieb, "On the construction and analysis of absorbing layer in CEM," Appl. Numer. Math. **27,** 331-340 (1998).
24. S. Abarbenel and D. Gottlieb, and J. S. Hesthaven, "Well-posed perfectly matched layers for advective acoustics," J. Comput. Phys. **154,** 266-283 (1999).
25. M. Born and E. Wolf, *Principles of Optics*, 7th ed. (Cambridge University Press, Cambridge, 1999), pp. 724-726.
26. S. R. Rengarajan and Y. Rahmat-Samii, "The field equivalence principle illustration of the establishment of the non-intuitive null fields," IEEE Antennas Propagat. Mag., **42**, 122-128 (2000).
27. R. S. Elliott, *Antenna theory and design* (Prentice-Hall, New Jersey, 1981), pp. 114-117.
28. M. Pelton, J. Aizpurua, and G. Bryant, "Metal-nanoparticle plasmonics," Laser & Photon. Rev. **2**, 136-159 (2008).
29. E. Hao and G. C. Schatz, "Electromagnetic fields around silver nanoparticles and dimmers," J. Chem. Phys. **120**, 357-366 (2004).
30. L. A. Sweatlock, S. A. Maier, H. A. Atwater, J. J. Penninkhof, and A. Polman, "Highly confined electromagnetic fields in arrays of strongly coupled Ag nanoparticles," Phys. Rev. B **71**, 235408:1-7 (2006).
31. A. V. Zayats, I. I. Smolyaninov, and A. A. Maradudin, "Nano-optics of surface plasmon polaritons," Phys. Rep. **408**, 131-314 (2005).
32. T. Setälä, M. Kaivola, and A. T. Friberg, "Evanescent and propagating electromagnetic fields in scattering from point-dipole structures," J. Opt. Soc. Am. A **18**, 678-688 (2001).
33. E. Wolf and J. T. Foley, "Do evanescent waves contribute to the far field?" Opt. Lett. **23**, 16-18 (1998).

1. Introduction

Plasmonics, as a newly developing field [1] owing to the rapid progress of nanofabrication technology, roots in the collective electromagnetic resonance of free electrons inside nanometer-scaled structures and creates many potential applications. One of the central research topics in plasmonics is to produce anomalous optical properties by tailoring the electromagnetic interaction among nanostructures. Especially, uniformly stable surface-enhanced Raman scattering (SERS) measurements have been demonstrated on

#110633 - $15.00 USD Received 27 Apr 2009; revised 7 Jul 2009; accepted 13 Jul 2009; published 31 Jul 2009

sculpted metallic surfaces made by Ag nanoparticle arrays embedded in anodic aluminum oxide (AAO) [2], because of its highly uniform enhanced local field residing between adjacent Ag nanoparticles (so called "hot spot"). The development of these SERS substrates thus greatly facilitates the application of Raman spectroscopy to sensitive chemical and biomedical sensors. For example, rapid and accurate diagnosis for pathogens and their antibiotic susceptibility based on these substrates has been demonstrated and is potentially critical for controlling bacterial infections [3]. These successful demonstrations thus urge a need to investigate the fundamental optical processes taking place in SERS based on these substrates. Light scattering spectra from the arrays, emulating these optical processes, were found to evolve with the gaps between adjacent nanoparticles. The observed spectral properties match with analytical formulae that were developed based on quasi-static dipole coupling model [4]. This study has thus revealed how the plasmonic coupling in the Ag nanoparticle array influences the light scattering in far zone, which is also taking place in performing Raman scattering on these substrates. A question then emerges: how is this near-field sensitive SERS phenomenon connected to the far-field scattering characteristics? More specifically, what is the near-field origin of the observed far-field scattering spectra that have been interpreted successfully by dipole-dipole coupling between Ag nanoparticles? The answers to these questions rely on near-field experimental studies [5] as well as high accuracy electrodynamic calculation.

Several numerical methods to solve Maxwell's equations have been developed to investigate the near-field electromagnetic interaction occurring within nanostructures. Zhao and coworkers have compared different calculation methods used to unravel the electromagnetic properties of plasmonic structures in a review article [6]. Among them, discrete dipole approximation (DDA) method [6] and finite-difference time-domain (FDTD) method [8] are two most commonly used methods. The DDA method computes scattering of radiation by an object based on the assumption that an ensemble of discrete dipoles can approximate the electrodynamic response of this continuum object on length scales that are large compared with the inter-dipole separation [7]. Although its computational effort is generally less than that for finite difference methods, the comparison of DDA results with Mie theory [9] indicates that errors in far-field results can reach 10%, suggesting that the error in near field can be even larger [6]. The FDTD method is a finite difference method and discretizes the electrodynamic wave equations based on Yee scheme [10]. Most importantly, this method divides the calculation domain into normal Cartesian cubes in three-dimensional cases, thus creating stair-cased representations of material interfaces leading to inaccurate computations in near field. Even with the use of local sub-grid method [11] for improving the accuracy of the simulated fields near curved interfaces, the FDTD method classified as a low-order accuracy method, may not be a computation loading efficient method to preserve the numerical accuracy for the long-time wave evolutions in multidimensional space, due to the accumulation of dispersive error during long-time integration [12]. The comparison with Mie theory shows a relative near-field error of ~2% at a distance of 2.5 nm away from the surface of an Au sphere [13]. The error is expected to drastically increase as the measurement point is directly on the surface. These comparison evidences indicate that it is important to use a high precision electrodynamic solver to obtain accurate near-field distribution under electromagnetic resonance for near-field investigation and applications, such as SERS [2], tip-enhanced Raman scattering [14], and plasmon-induced fluorescence quenching and enhancement [15]. In particular, high-order accuracy element-wise computing approaches, like the discontinuous Garlerkin finite element methods [16] and the multi-domain pseudospectral methods [17], adopt flexible geometrical shape elements to well fit possible curved boundaries and use high-order accurate computing algorithms to simulate fields with boundary conditions imposed correctly within each element. In the present simulation study, we employ a multi-domain pseudospectral computational framework in time domain, so called pseudo-spectral time-domain (PSTD) method, adopted with a dispersive

#110633 - $15.00 USD Received 27 Apr 2009; revised 7 Jul 2009; accepted 13 Jul 2009; published 31 Jul 2009

material computational model to investigate both near- and far-field optical properties of Ag nanoparticle arrays grown in self-organized AAO nanochannels [2, 4], seeking out their unresolved relationship in this plasmonic structure.

The sections below are organized as follows. The geometry of Ag nanorod arrays adopted in the simulation and the numerical scheme based on PSTD method to solve dispersive Maxwell equations are delineated in Sec. 2. Furthermore, the computational error is illustrated by the comparison with Mie theory. Section 3 presents the scattering spectra of the arrays with different gaps as well as their corresponding near-field distributions. The implication of this simulation study to the use of these arrays in SERS applications is discussed. Finally, Section 4 concludes the main results of this study.

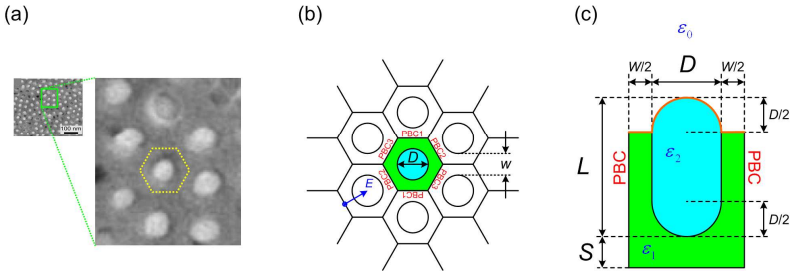

Fig. 1. Top-view scanning electron microscopy image (a) and top-view (b) and side-view (c) schematic diagrams of Ag/AAO substrate. The blue arrow represents the electric field direction of incident light wave. PBC and PBC1~3 represent periodic boundary conditions. D and L are the diameter and length of Ag nanorods, respectively, while W is the gap between adjacent nanorods. S is the distance from the bottom of the Ag nanorod to the bottom surface of alumina. ε_0, ε_1 and ε_2 are dielectric functions of vacuum, alumina, and silver, respectively. Orange line represents the top surface of the substrate.

2. Numerical scheme and calculation geometry

Figure 1 shows a top-view scanning electron microscopy image of a typical Ag/AAO substrate, as well as the corresponding top- and side-view schematic diagrams which are drawn based on our previous experimental work [4]. The Ag nanorods with a diameter of D and a length of L are arranged in a hexagonal pattern with an inter-nanorod gap of W, and are embedded inside alumina matrix with only the half-sphere round top exposed in vacuum, as shown in Fig. 1(c). Although there exist some inhomogeneous variations in D, L, W as well as the proportion of the rod exposed in vacuum [2, 4], all the calculations performed were carried out with the mean values of these dimensions to simplify the simulation. Discussion will be given later about the influence of the inhomogeneities. In this study, D and L were set to be 25 and 100 nm, respectively, and five different gaps (5, 10, 15, 20, 25 nm) were chosen to simulate the experimental condition. To fully incorporate the dispersive property of Ag over the spectral range of interest ranging from 400 to 800 nm into the adopted numerical model, its dielectric function is represented as a Drude-Lorentz model expressed by

$$\varepsilon_{DL}(\omega) = \varepsilon_\infty - \frac{\omega_p^2}{\omega(\omega + i/\tau_D)} + \sum_{s=1}^{v} \frac{f_s \omega_p^2}{(\omega_s^2 - \omega^2) - i\omega\Gamma_s}, \quad (1)$$

where ε_∞ is the high-frequency limit of the dielectric constant, ω_p and τ_D are the plasma frequency and the life time in the Drude model of metal, respectively, v is the number of Lorentz oscillators with a natural frequency of ω_s, a strength of f_s, and a damping constant of Γ_s in the Lorentz model to account for possible interband transitions in metal. Two Lorentz terms are adopted to accurately represent the experimental data taken from the work by Lynch and Hunter [18] during the parameter extraction process. Its

#110633 - $15.00 USD Received 27 Apr 2009; revised 7 Jul 2009; accepted 13 Jul 2009; published 31 Jul 2009

detailed consideration is delineated in the Appendix. The dielectric constant of alumina was set to be 3 over the spectral range of interest [4, 19].

Based on the Drude-Lorentz model, Eq. (1), dispersive Maxwell's equations were derived according to the auxiliary differential equation (ADE) technique [8, 20], owing to its efficiency of memory usage. The resultant governing equations in the metallic medium are

$$\nabla \times \vec{\mathcal{H}} = \varepsilon_\infty \frac{\partial}{\partial t}\vec{\mathcal{E}} + \sum_{s=1}^{2} \frac{\partial}{\partial t}\vec{\mathcal{P}}_s + \vec{\jmath}, \tag{2a}$$

$$\nabla \times \vec{\mathcal{E}} = -\mu \frac{\partial}{\partial t}\vec{\mathcal{H}}, \tag{2b}$$

$$\nabla \cdot \vec{\mathcal{E}} = -\frac{1}{\varepsilon_\infty} \sum_{s=1}^{2} \nabla \cdot \vec{\mathcal{P}}_s, \tag{2c}$$

and

$$\nabla \cdot \vec{\mathcal{H}} = 0 \tag{2d}$$

with the following three dynamical equations reflecting the Drude-Lorentz model shown in Eq. (1):

$$\frac{\partial}{\partial t}\vec{\jmath} + \tau_D^{-1}\vec{\jmath} = \omega_p^2 \vec{\mathcal{E}} \tag{2e}$$

and

$$\frac{\partial^2}{\partial t^2}\vec{\mathcal{P}}_s + \Gamma_s \frac{\partial}{\partial t}\vec{\mathcal{P}}_s + \omega_s^2 \vec{\mathcal{P}}_s = f_s \omega_p^2 \vec{\mathcal{E}} \quad \{s = 1 \text{ and } 2\}, \tag{2f}$$

where $\vec{\mathcal{E}}$ and $\vec{\mathcal{H}}$ are the electric and magnetic fields, respectively, $\vec{\mathcal{P}}_s$ is the polarization corresponding to the s-th Lorentz term, and $\vec{\jmath}$ is the electric current density within the metal medium.

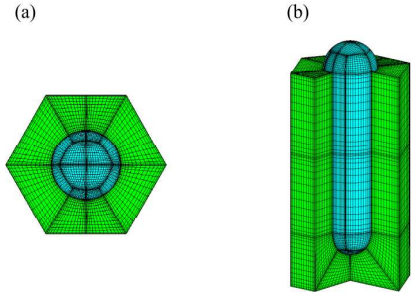

Fig. 2. (a) Top-view and (b) side-view of mesh scheme of single unit cell used in calculation. The diameter and the length of the Ag nanorod are 25 and 100 nm, respectively, and the inter-nanorod gap is 25 nm.

The approach used to solve Eqs. (2) has been delineated in detail previously [17]. Briefly, the physical domain of the unit cell, illustrated as an example of the Ag nanorod array with W = 25 nm in Fig. 2, was first decomposed into a series of non-overlapping, curved hexahedral sub-domains. These sub-domain blocks in x-space were then mapped one-to-one into a unit cube in ξ-space. Secondly, a collocation method based on Legendre-Gauss-Lobatto (LGL) quadrature points was used to construct Legendre-Lagrange interpolation polynomials to accurately evaluate the field and its derivatives at these sampling points of the unit cube. The number of the sampling points on each edge of individual sub-domain, N_S, is 15 and the resultant mesh grids in x-space in the array of W = 25 nm are shown in Fig. 2. Thirdly, a low-storage fourth-order five-stage Runge-Kutta algorithm [21]

#110633 - $15.00 USD Received 27 Apr 2009; revised 7 Jul 2009; accepted 13 Jul 2009; published 31 Jul 2009

was applied in temporal discretization for efficient memory use, as compared with the standard fourth-order Runge-Kutta scheme. Moreover, time-explicit boundary conditions in treating the input external electromagnetic wave at the Runge-Kutta intermediate stages [22] were used to ensure high accuracy. Finally, two proper absorbing boundary layers [17, 23, 24], which includes a top absorbing bounding layer located 75 nm above the top surface of alumina and a bottom absorbing boundary layer located 50 nm below the bottom surface of alumina, were applied to prevent the reflective waves from interfering with the numerical results. In order to treat the approximately infinite Ag nanorod array, three periodic boundary conditions were applied on the sidewalls of the hexagonal unit cell (Fig. 1).

The pseudospectral penalty scheme in the semi-discrete level used in the calculation takes the following form:

$$M_{ijk}^{(1)}\frac{\partial q_{ijk}^{(1)}}{\partial t}=-\sum_{\eta=1}^{3}A_{\eta}^{(1)}\frac{\partial q_{ijk}^{(1)}}{\partial \xi_{\eta}}-C^{(1)}q_{ijk}^{(2)}-\frac{\chi}{2}P_{ijk}, \tag{3a}$$

$$M_{ijk}^{(2)}\frac{\partial q_{ijk}^{(2)}}{\partial t}=-C^{(2)}q_{ijk}^{(1)}-C^{(3)}q_{ijk}^{(2)}, \tag{3b}$$

where $q_{ijk}^{(1)}(t)=\left(\mathcal{E}_x,\mathcal{E}_y,\mathcal{E}_z,\mathcal{H}_x,\mathcal{H}_y,\mathcal{H}_z\right)^T\left(\xi_{ijk},t\right)$,

$$q_{ijk}^{(2)}(t)=\left(\mathcal{J}_x,\mathcal{J}_y,\mathcal{J}_z,\mathcal{Q}_{x,1},\mathcal{Q}_{y,1},\mathcal{Q}_{z,1},\mathcal{Q}_{x,2},\mathcal{Q}_{y,2},\mathcal{Q}_{z,2},\mathcal{P}_{x,1},\mathcal{P}_{y,1},\mathcal{P}_{z,1},\mathcal{P}_{x,2},\mathcal{P}_{y,2},\mathcal{P}_{z,2}\right)^T\left(\xi_{ijk},t\right),$$

χ is a free parameter to stabilize the scheme. $\mathcal{Q}_{r,s}=\partial\mathcal{P}_{r,s}/\partial t$, where r = x, y and z. Furthermore, $M_{ijk}^{(1)}=\mathrm{diag}\left[\varepsilon_\infty,\varepsilon_\infty,\varepsilon_\infty,\mu_0,\mu_0,\mu_0\right]$, where μ_0 is permeability of vacuum. $M_{ijk}^{(2)}=\mathrm{I}_{15\times15}$ and

$$A_{\eta}^{(1)}=\begin{bmatrix}0&0&0&0&\delta_{\eta3}&-\delta_{\eta2}\\0&0&0&-\delta_{\eta3}&0&\delta_{\eta1}\\0&0&0&\delta_{\eta2}&-\delta_{\eta1}&0\\0&-\delta_{\eta3}&\delta_{\eta2}&0&0&0\\\delta_{\eta3}&0&-\delta_{\eta1}&0&0&0\\-\delta_{\eta2}&\delta_{\eta1}&0&0&0&0\end{bmatrix},$$

where δ_{ij} is Kronecker delta function.

$$C^{(1)}=\begin{pmatrix}\mathrm{I}_{3\times3}&\mathrm{I}_{3\times3}&\mathrm{I}_{3\times3}&0_{3\times6}\\0_{3\times3}&0_{3\times3}&0_{3\times3}&0_{3\times6}\end{pmatrix},\quad C^{(2)}=\begin{Bmatrix}-\left[\omega_p^2\right]_{3\times3}&-\left[f_1\omega_p^2\right]_{3\times3}&-\left[f_2\omega_p^2\right]_{3\times3}&0_{6\times3}\\0_{3\times3}&0_{3\times3}&0_{3\times3}&0_{6\times3}\end{Bmatrix}^T,$$

and

$$C^{(3)}=\begin{pmatrix}\left[\tau^{-1}\right]_{3\times3}&0_{3\times3}&0_{3\times3}&0_{3\times3}&0_{3\times3}\\0_{3\times3}&\left[\Gamma_1\right]_{3\times3}&0_{3\times3}&\left[\omega_2^2\right]_{3\times3}&0_{3\times3}\\0_{3\times3}&0_{3\times3}&\left[\Gamma_2\right]_{3\times3}&0_{3\times3}&\left[\omega_2^2\right]_{3\times3}\\0_{3\times3}&-\mathrm{I}_{3\times3}&0_{3\times3}&0_{3\times3}&0_{3\times3}\\0_{3\times3}&0_{3\times3}&-\mathrm{I}_{3\times3}&0_{3\times3}&0_{3\times3}\end{pmatrix},$$

where $\mathrm{I}_{n\times m}$ and $0_{n\times m}$ denote identity and zero matrices with n rows and m columns, respectively. $\left[*\right]_{n\times m}=\mathrm{diag}\left[*,*,*\right]$, where $*$ is any element in { ω_p^2, ω_s^2, $f_s\omega_p^2$, τ_D^{-1},

#110633 - $15.00 USD Received 27 Apr 2009; revised 7 Jul 2009; accepted 13 Jul 2009; published 31 Jul 2009

Γ_s }. Note that the boundary conditions to be imposed on the boundary surfaces of each sub-domain are absorbed in P_{ijk} of Eq. (3a), called the penalized terms that serve mainly to exchange the information between adjacent boundary surfaces of surrounding sub-domains and to stabilize the numerical scheme. The explicit expressions of the penalized terms for different types of boundary conditions and the proper value of the penalty parameter χ for stable computations can be founded in Ref. 17. Notice that the divergence constraints in Eqs. (2c) and (2d) are not involved in the computations. This is due to the well known fact that the divergence constraints are satisfied at all times provided that they are fulfilled initially. Since vanishing fields ($\vec{\mathcal{E}} = 0$, $\vec{\mathcal{P}} = 0$, and $\vec{\mathcal{H}} = 0$) that automatically satisfy these constraints were taken as initial conditions in our computations, we only need consider discretizing the curl equations, Eqs. (2a) and (2b), and the dispersive model equations, Eqs. (2e) and (2f).

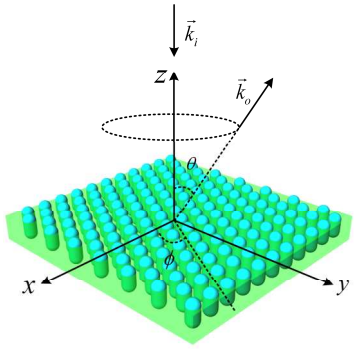

Fig. 3. Incident-and-scattering geometry over an array of Ag nanorods arranged in a hexagonal pattern. $\vec{k}_i$ and $\vec{k}_o$ are the wave vectors of incident and scattered waves, respectively. θ is scattering collection angle.

In the un-polarized dark-field scattering study published previously [4], the excitation light wave was incident to the substrate surface at 45° in a cone-shape manner while the backward scattering light was collected along the surface normal direction. To simplify the calculation effort, the incident light direction was, on the other hand, chosen to be normal to the surface, while the scattering light was collected around the cone at $\theta = 45°$. According to the reciprocity theorem of electromagnetics [25], the calculated scattered spectrum is identical to that obtained in the experimental geometry. Furthermore, the electric field strength of the incident wave was set to be one for simplicity. Figure 3 depicts the incident wave and the scattering collection geometry used in the calculation over an array of Ag nanorods that is embedded in the AAO substrate and is arranged in the hexagonal pattern. The *x*-axis is along the direction in which two adjacent nanorods are closest. As described above, to avoid simulating the whole array, a hexagonal unit cell with periodic boundary conditions (PBCs), as shown in Figs. 1(b) and (c), was used to save calculation time, assuming that the excitation source is a plane wave.

The calculation of the scattering cross section, σ_{SC}, was realized with the use of the near-to-far-field transformation developed based on the field equivalence principle [26]. First, both $\vec{E}$ and $\vec{H}$ on the top surface of the Ag nanorod array, shown in Fig. 1(c), in frequency domain were calculated by performing Fourier transform of $\vec{\mathcal{E}}$ and $\vec{\mathcal{H}}$ in time domain, separately. The corresponding electric and magnetic current densities (denoted by $\vec{J}$ and $\vec{M}$, respectively) in frequency domain on the top surface of the array, Fig. 1(c), were subsequently calculated with the following two relations:

#110633 - $15.00 USD Received 27 Apr 2009; revised 7 Jul 2009; accepted 13 Jul 2009; published 31 Jul 2009

$$\vec{J} = \hat{n} \times \vec{H} \tag{4a}$$

and

$$\vec{M} = -\hat{n} \times \vec{E}, \tag{4b}$$

where $\hat{n}$ is the normal vector on the top surface. Through Green's functions, the electric and magnetic vector potentials were then obtained to produce far-field components. In the numerical calculation of σ_{SC}, we followed its notation used in Ref. 7 and considered the total contribution of nanorod arrays by adding array factors [27]. As a result, σ_{SC} can be expressed as

$$\sigma_{SC}(k,\theta,\phi) \equiv \lim_{R\to\infty}\left(4\pi R^2 \frac{P_{SC}}{P_{IN}}\right) = \frac{k^2}{8\pi\eta_0 P_{IN}}\left(\left|L_\phi + \eta_0 N_\theta\right|^2 + \left|L_\theta - \eta_0 N_\phi\right|^2\right) \tag{5}$$

with

$$N_\theta = \int_S \left(J_x \cos\theta\cos\phi + J_y \cos\theta \sin\phi - J_z \sin\theta\right) \times e^{jk(\hat{r}\cdot\vec{r}_0)} \Theta(k,\theta,\phi)\, ds,$$

$$N_\phi = \int_S \left(-J_x \sin\phi + J_y \cos\phi\right) \times e^{jk(\hat{r}\cdot\vec{r}_0)} \Theta(k,\theta,\phi)\, ds,$$

$$L_\theta = \int_S \left(M_x \cos\theta\cos\phi + M_y \cos\theta \sin\phi - M_z \sin\theta\right) \times e^{jk(\hat{r}\cdot\vec{r}_0)} \Theta(k,\theta,\phi)\, ds,$$

and

$$L_\phi = \int_S \left(-M_x \sin\phi + M_y \cos\phi\right) \times e^{jk(\hat{r}\cdot\vec{r}_0)} \Theta(k,\theta,\phi)\, ds,$$

where P_{IN} and P_{SC} are the power densities of the incident and scattered waves, respectively, k is the wavenumber in free space, S is the top surface of the unit cell, as shown in Fig. 1(c), $\hat{r} = (\sin\theta\cos\phi, \sin\theta\sin\phi, \cos\theta)$, $\vec{r}_0$ stands for the source point vector with respect to the origin within the unit cell, and η_0 is the intrinsic impedance of vacuum. The array factor for a hexagonal periodic pattern is expressed as

$$\Theta(k,\theta,\phi) = \lim_{N\to\infty} \sum_{m=-N}^{N} \sum_{n=-N}^{N} A \exp\left(jk\sin\theta\left[\left(ma + na\cos 60^\circ\right)\cos\phi + na\sin 60^\circ \sin\phi\right]\right),$$

where A denotes the amplitude contribution for each unit cell, as all the unit cells are identical. $a\ (= D + W)$ is the inter-nanorod spacing. As the illuminating area on the sample in the scattering experiments was approximately a square covering about 1 μm^2, the number of nanorods was estimated accordingly for each array. Finally, the total scattering field was obtained by integrating over ϕ along the circular path in Fig. 3 to simulate the far-field scattering measurement configuration.

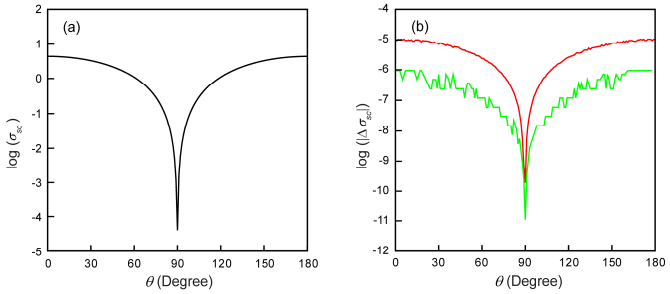

#110633 - $15.00 USD Received 27 Apr 2009; revised 7 Jul 2009; accepted 13 Jul 2009; published 31 Jul 2009

Fig. 4. (a) Bistatic scattering cross section (σ_{SC}) *vs*. observation angle, θ, for a silver sphere with a diameter of 25 nm at $\phi = 0°$ and (b) errors ($|\Delta\sigma_{SC}|$) for N = 13 (red line) and 15 (green line).

The scattering calculation of a silver sphere in aluminum oxide, so called Mie scattering problem [9], was also performed to test the accuracy of the implemented numerical scheme. The detail to obtain the corresponding σ_{SC} is given below. The diameter of the sphere was set at 25 nm and the wavelength of the incident wave was chosen to be λ_R (= 0.47 μm) at which the scattering intensity reaches maximum. Figure 4 shows the calculated σ_{SC} and the difference between the exact result from the Mie theory and the calculated value, $|\Delta\sigma_{SC}|$, as a function of the observation angle, θ. Notice that $|\Delta\sigma_{SC}|$ for $N_S = 15$ is less than 10^{-6}. Furthermore, the maximal error of the field components on the surface of the sphere is less than 3×10^{-3}, which corresponds to a maximal energy error of 10^{-5}. This result is much smaller than the corresponding one obtained with the FDTD method [13].

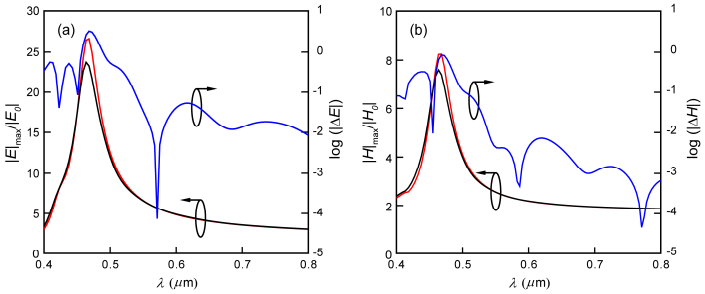

Fig. 5. Maximal (a) electric and (b) magnetic fields ($|E|_{max}$ and $|H|_{max}$, respectively) on the surface of a silver sphere embedded in alumina as a function of wavelength, λ. The diameter of the sphere is 25 nm. Black lines represent calculated results based on the dielectric function of silver, red lines represent that based on fitted Drude-Lorentz model, and blue lines represent the difference between them ($|\Delta E|$ and $|\Delta H|$).

Another important issue involved in the effort of matching the calculation results with the experimental ones in the electrodynamic simulation of plasmonics is how the mismatch between them depends on the distinction of the fitted Drude-Lorentz model from the actual dielectric function of silver. Figure 5 shows the maximal electric and magnetic field strengths on the surface of the silver sphere as a function of the wavelength of the incident wave, which were calculated according to Mie theory with the two dielectric functions. Notice that the maximal differences for both electric and magnetic fields, $|\Delta E|$ and $|\Delta H|$, occur at λ_R reach about 10%, while the differences in percentage decrease dramatically as the wavelength moves away from λ_R. On the other hand, the differences between the actual dielectric function of silver and the fitted value of both the real and imaginary parts at λ_R are only about 2.5% (Appendix A), indicating that plasmonic resonance magnifies the introduced error of the dielectric function in the calculation. This comparison study illustrates the importance of the accuracy of the dielectric functions of metal used in the near-field calculation of electromagnetic properties of plasmonic structures.

3. Results and discussion

Figure 6 shows the calculated far-field spectra of Ag nanorod arrays with five different inter-nanorod gaps (5, 10, 15, 20, and 25 nm) for *x*- and *y*-polarized incident light waves. I_{SC} represents the far-field scattering intensity normalized to its maximal value. Notice that

#110633 - $15.00 USD Received 27 Apr 2009; revised 7 Jul 2009; accepted 13 Jul 2009; published 31 Jul 2009

the resonance peak wavelength increases and the resonance width is broadened as the gap decreases, which is qualitatively consistent with our experimental observation published previously [4]. In particular, the center wavelength of the resonance feature for the Ag nanorod array with a 5-nm gap is located approximately at 600 nm that also agrees with the corresponding experimental data. The good correspondence between the numerical calculation and the experimental results delivers three important messages. First, the Ag nanorod arrays were accurately represented by the structures used for calculation. Second, the developed electrodynamic simulation approach based on the PSTD method used in this study can truthfully simulate the optical behaviors of these arrays. Third, the agreement gives us great confidence to utilize this simulation approach to investigate the fundamental nature of electromagnetic interaction occurring among these Ag nanorods.

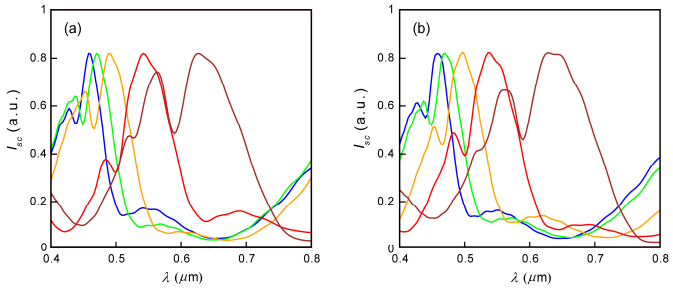

Fig. 6. Normalized scattering intensity spectra in (a) *x*-polarized and (b) *y*-polarized excitation schemes of Ag nanorod arrays with five different inter-nanorod gaps: 5 (brown lines), 10 (red lines), 15 (orange lines), 20 (green lines) and 25 nm (blue lines).

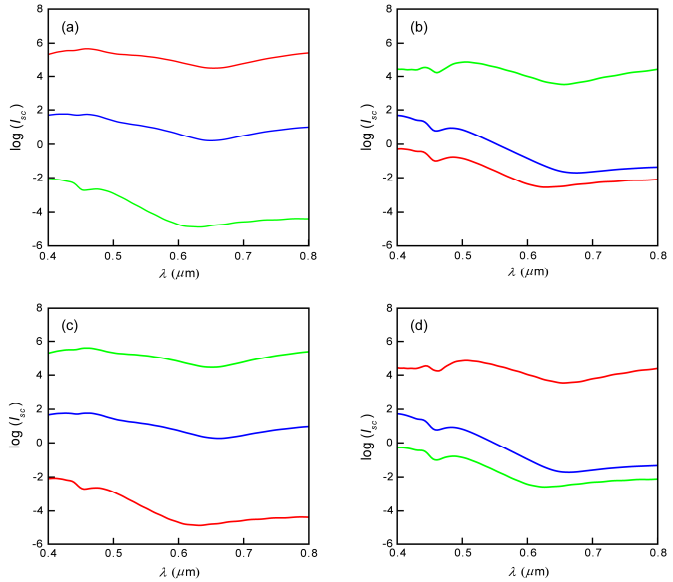

Fig. 7. Scattering intensity contribution of surface current densities in *x*-polarized excitation scheme as a function of wavelength, λ: (a) $\vec{J}$ and (b) $\vec{M}$; corresponding one in *y*-polarized excitation scheme: (c) $\vec{J}$ and (d) $\vec{M}$. Red lines represent the *x*-component, Green lines represent the *y*-component, and blue lines represent the *z*-component.

In addition to the three main inferences achieved from the calculation results shown in Fig. 6, there are several other related points that are worthy of mentioning. First, the short-wavelength scattering tail close to 400 nm appearing in the experimental data is missing in the simulated data. This is most likely due to the fact that the surface of the fabricated

#110633 - $15.00 USD Received 27 Apr 2009; revised 7 Jul 2009; accepted 13 Jul 2009; published 31 Jul 2009

samples is not smooth, enhancing the strength of Rayleigh scattering at short wavelengths. Second, another distinct spectral feature in the simulated data is that a long-wavelength peak at approximately 1 μm is present in all the simulated scattering spectra (not shown in Fig. 6). Our simulation test on an array with a rod length of 50 nm shows that the long-wavelength peak is blue-shifted, indicating that it corresponds to the longitudinal resonance mode of the Ag nanorods. Third, characteristic dips exist in the calculated scattering spectra, while they are absent in the corresponding experimental results. This difference may be due to the fact that the inhomogeneous distribution of the inter-nanorod gap existing in the samples owing to fabrication imperfection [4] can easily remove this characteristic spectral feature. Finally, the far-field scattering spectra of the two excitation polarization schemes are similar in both the spectral features (resonance peak wavelength and width). This property was similarly obtained in our previous theoretical derivation based on quasi-static dipole model [4]. The agreement between the calculation results and the theoretical derivation suggests that the hexagonal packing configuration represents a relatively uniform two-dimensional distribution of Ag nanorods, making the polarization-dependent spectral character almost invisible.

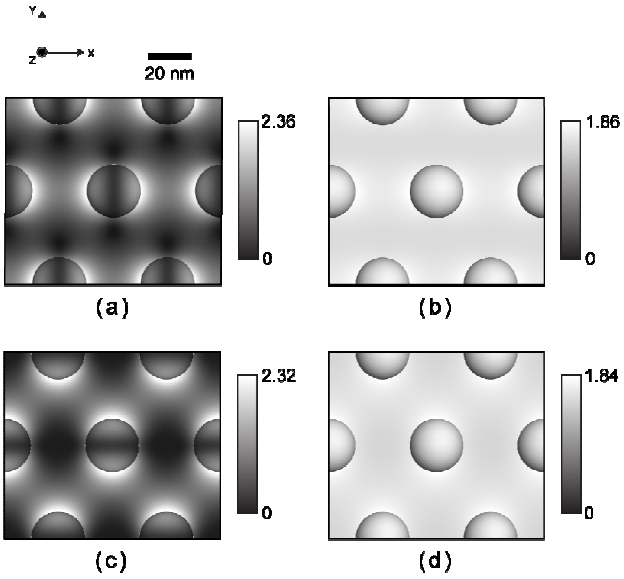

Fig. 8. Surface field distribution of Ag nanorod array with W = 25 nm at λ = 626 nm in x-polarized excitation scheme: (a) electric and (b) magnetic field, and corresponding ones in y-polarized excitation scheme: (c) electric and (d) magnetic field.

The correspondence between the experimental and calculation results renders us great confidence to identify the near-field origins of the observed far-field scattering spectra and to interrogate the electromagnetic interaction that evokes them. According to the field equivalence principle [26], both $\vec{J}$ and $\vec{M}$ on the top surface of the Ag nanorod arrays are the sources in the calculation of distant scattering fields. Figures 7(a) and (b) show the scattering intensity of each Cartesian component of the two surface current densities for the Ag nanorod array with W = 25 nm in the x-polarized excitation scheme, where the polarization of the incident optical wave is parallel with the x-axis. Notice that the total scattering intensity in far field is mainly contributed by J_x and M_y and, furthermore, the contribution by J_x is several times of that by M_y. In contrast, J_y and M_x play the dominant role in the y-polarized excitation scheme and the contribution by J_y is similarly larger than that by M_x as shown in Figs. 7(c) and (d). For the cases of other gaps, the same components also consistently dominate the far-field scattering intensity spectra. One question then emerges

#110633 - $15.00 USD Received 27 Apr 2009; revised 7 Jul 2009; accepted 13 Jul 2009; published 31 Jul 2009

naturally: does this behavior only exist in the 45°-scattering geometry? The calculations of the scattering angles at 0° and 90° were performed similarly and show the same behavior, indicating that this surface electric current dominated character is genuine in nature for these Ag nanorod arrays.

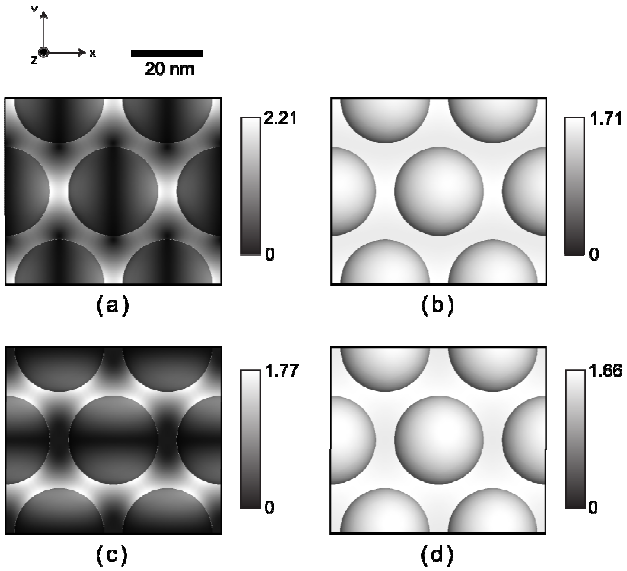

Fig. 9. Surface field distribution of Ag nanorod array with W = 25 nm at λ = 629 nm in x-polarized excitation scheme: (a) electric and (b) magnetic field, and corresponding ones in y-polarized excitation scheme: (c) electric and (d) magnetic field.

As $\vec{J}$ and $\vec{M}$ were calculated by surface magnetic and electric fields according to Eq. (4), respectively, it is thus of great help to discuss the behaviors of the two surface fields to understand the reason why $\vec{J}$, instead of $\vec{M}$, dominates the far-field scattering. Figures 8(a) and (b) show the surface $|\vec{E}|$ and $|\vec{H}|$ at 458 nm, respectively, that give the maximal scattering intensity in the case of W = 25 nm in the x-polarized excitation scheme. Notice that the surface $|\vec{E}|$ is localized at the two ends of the Ag nanorods along the x-axis, which is consistent with the expected local electric field distribution of an isolated dipole-like Ag nanorod at electromagnetic resonance [28]. On the other hand, the surface $|\vec{H}|$ is delocalized over the whole surface and produces the corresponding $\vec{J}$ that acts as the dominant source of the far-field scattering of our Ag nanorod arrays. The distribution of the surface $|\vec{H}|$ can be similarly observed in our calculation of Mie scattering described above. The two observations above thus provide the first important conclusion resulting from this study: the surface magnetic field of these Ag nanorod arrays produces the near-field current source that dominates the far-field scattering. In comparison, Figs. 8(c) and (d) show the surface $|\vec{E}|$ and $|\vec{H}|$ at the same wavelength, respectively, in the case of W = 25 nm in the y-polarized excitation scheme. The surface $|\vec{E}|$ is localized at the two ends of the Ag nanorods along the y-axis and the surface $|\vec{H}|$ is also delocalized over the whole surface. As the gap decreases, the plasmonic coupling between adjacent Ag nanorods is enhanced as in the case of the x-polarized excitation scheme. As an example, Figs. 9(a) and (b) show the

#110633 - $15.00 USD Received 27 Apr 2009; revised 7 Jul 2009; accepted 13 Jul 2009; published 31 Jul 2009

surface $|\vec{E}|$ and $|\vec{H}|$ at 626 nm, respectively, that gives the maximal scattering intensity in the case of W = 5 nm in the x-polarized excitation scheme. Notice that the surface $|\vec{E}|$ extends over the region between adjacent Ag nanorods along the x-axis, creating so-called "hot spots." This local enhanced electric field was similarly obtained previously in nanoparticle dimers [29], linear nanosphere chains [30], etc. The surface $|\vec{H}|$ in this case spreads even more uniform over the whole surface than that in the case of W = 25 nm. In comparison, Figs. 9(c) and (d) show the surface $|\vec{E}|$ and $|\vec{H}|$ at 629 nm, respectively, in the case of W = 5 nm in the y-polarized excitation scheme. The surface $|\vec{E}|$ is mainly localized in the gap region along the two directions that are 30° with respect to the y-axis, because the electric field component of the incident wave along the two directions is the largest. On the other hand, the surface $|\vec{H}|$ almost evenly covers the whole surface, just as the case in the x-polarized excitation scheme.

The drastically distinct distributions of the surface $|\vec{E}|$ and $|\vec{H}|$ illustrated above for all the Ag nanorod arrays can be comprehended on the basis of quasi-static dipole model [4]. Under plasmon resonance, free electrons inside an isolated Ag nanorod undergo collectively oscillatory motion (dipole), yielding the enhanced localized electric field at its two polar ends that is aligned with the polarization of the incident optical wave, $\vec{e}$. The concurrent magnetic field, on the other hand, surrounds the surface of the Ag nanorod, owing to the induced linear oscillatory electron motion along $\vec{e}$. In the case of an isolated Ag nanorod dimer with a very small gap and the dimer axis is parallel with $\vec{e}$, plasmonic coupling taking place between them synchronizes the motions of the free electrons inside the two individual nanorods, extending the localized electric field, *per se*, into the gap region and simultaneously aligning the oscillatory electrons in the two separate nanorods. The two in-phase oscillatory dipoles similarly expand the magnetic field over the region enclosing the dimer. Finally, by the same token, the plasmonic coupling in the case of two-dimensional Ag nanorod arrays brings all the dipole oscillations in phase and thus eventually makes the magnetic field spread almost uniformly over the whole surface. The closer the inter-nanorod gap is, the more uniform the surface magnetic field is over the top surface. In comparison, despite the successful interpretation of the far-field scattering properties in our previous work [4], the adopted dipole coupling model conceals the near-field to far-field correspondence.

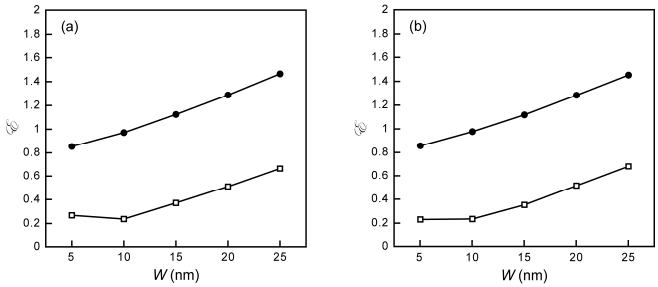

Fig. 10. Average energy densities, $\bar{w}$, on the top surface of the Ag nanorod arrays as a function of the inter-nanorod gap, W, at resonance corresponding to surface electric (open squares) and magnetic field (filled circles) in x-polarized (a) and y-polarized (b) excitation schemes.

A close examination of the average energy densities over the top surfaces of the Ag nanorod arrays also can shed light on the nature of these surface fields. Figure 10 shows the

#110633 - $15.00 USD Received 27 Apr 2009; revised 7 Jul 2009; accepted 13 Jul 2009; published 31 Jul 2009

surface average energy density, $\mathscr{E}$, as a function of the inter-nanorod gaps at their respective resonance wavelengths in the two polarization excitation schemes, where

$$\mathscr{E} = \frac{1}{2}\int_S \varepsilon_0 \left|\vec{E}\right|^2 ds \Big/ \int_S ds \text{ or } \frac{1}{2}\int_S \mu_0 \left|\vec{H}\right|^2 ds \Big/ \int_S ds,$$

corresponding to the surface $\left|\vec{E}\right|$ and $\left|\vec{H}\right|$, respectively, and S represents the top surface region. Notice that the energy density corresponding to the surface $\left|\vec{H}\right|$ is significantly larger than the one corresponding to the surface $\left|\vec{E}\right|$. This fact is thus consistent with the observation that the surface electric current dominates the far-field scattering intensity, as the scattering intensity in far zone directly reflects the field strength of the surface electric and magnetic fields. Furthermore, both the average surface electric and magnetic energy densities decrease with the decrease in the inter-nanorod gap. This behavior agrees with the predicted behavior of the Q factor of the arrays based on the quasi-static dipole coupling model published previously [4]. That is, the average electric and magnetic field strength is lower as the inter-nanorod gap becomes smaller, owing to the fact that the inter-nanorod energy transfer induced by plasmonic coupling expedites the energy dissipation caused by electron-phonon interaction within individual Ag nanorods.

It is quite surprising in the beginning about the presented conclusive evidence that the far-field scattering intensity is mainly contributed by the surface magnetic field in these Ag nanorod arrays. The roles of the surface electric and magnetic current densities are worthy of further discussion, because they may provide an in-depth view about the fundamental nature of the electromagnetic interaction within the Ag nanorod arrays as well as the intricate relation between the near-field distribution and the spectral characteristics in far-field scattering. First, according to the asserted field equivalence principle, $\vec{J}$ and $\vec{M}$ act as the virtual current sources on the boundary surface of an enclosed region in the calculation of the field exterior to the region. Although the acceptance of this principle has been rather bothersome and not comfortably realized [26], it has been popularly used in the electrodynamic calculation of radar cross section in the problems of electromagnetic scattering. In this study, these two virtual sources serve as a mediate role in the connection between the surface fields in near zone and the scattering fields in far zone, although they do not have direct physical meaning. Second, they can be used to determine the separate contributions of the sources located on the top surfaces of aluminum oxide and silver nanorod to the far-field scattering. Figure 11(a) shows the scattering intensity spectra of $\left|J_x\right|$ in the x-polarized excitation scheme from the top surface of aluminum oxide, $I_{SC}\left(\mathrm{AlO_x}\right)$, for the five different interparticle gaps, whereas that from the top surface of Ag nanorod, $I_{SC}\left(\mathrm{Ag}\right)$, are shown Fig. 11(b). Notice that the ratio between $I_{SC}\left(\mathrm{AlO_x}\right)$ and $I_{SC}\left(\mathrm{Ag}\right)$ at the resonance wavelength increases from about four for W = 25 nm to one for W = 5 nm. On the other hand, the area fraction of the Ag nanorod surface increases from 37% for W = 25 nm to 77% for W = 5 nm. The two extracted facts then indicate that the scattering contribution from the $\left|J_x\right|$ on the top surface of aluminum oxide is consistently larger than that on the top surface of Ag nanorod. The conclusion above is also reached in the y-polarized excitation scheme, as shown in Figs. 11(c) and (d). Third, the question why the far-field scattering contribution of $\left|\vec{J}\right|$ is larger than that of $\vec{M}$ can be answered by the variation of $\left|\vec{E}\right|$ and $\left|\vec{H}\right|$ above the top surface of the Ag nanorod array. As an example, Fig. 12 shows the cross-sectional view of $\left|\vec{E}\right|$ and $\left|\vec{H}\right|$ above the top surface of the Ag nanorod array with W

#110633 - $15.00 USD Received 27 Apr 2009; revised 7 Jul 2009; accepted 13 Jul 2009; published 31 Jul 2009

= 5 nm. Notice that $|\vec{H}|$ extends above the top surfaces of both the aluminum oxide and the Ag nanorod, whereas $|\vec{E}|$ concentrates in the gap region and decays in a short distance above the top surface. This behavior indicates that $|\vec{E}|$ has a more evanescent-wave character than $|\vec{H}|$ does, which is in great contrast to the corresponding near-field behavior of surface plasmon polaritons [30] where both $|\vec{E}|$ and $|\vec{H}|$ above surface have identical evanescent-wave property. Setälä, Kaivola and Friberg [32] investigated the propagating and evanescent field contributions in the far-field scattering of an array of electric point dipoles and showed that the near-field distribution of the propagating electric field is uniform while that of the calculated corrugated evanescent electric field reflects the positions of the dipoles. Their results have a close resemblance to the observed $|\vec{E}|$ here. Our calculation, in addition, shows that the surface $|\vec{H}|$ in the Ag nanorod arrays makes the dominant contribution in the observed propagating wave in far field, which has been largely ignored in the past. This result may thus impose a need to revise the traditional $|\vec{E}|$-dominated view of the characteristic optical properties of plasmonic structures and raises many interesting questions about the interpretation of the properties of plasmon-based optical devices, such as SERS substrates.

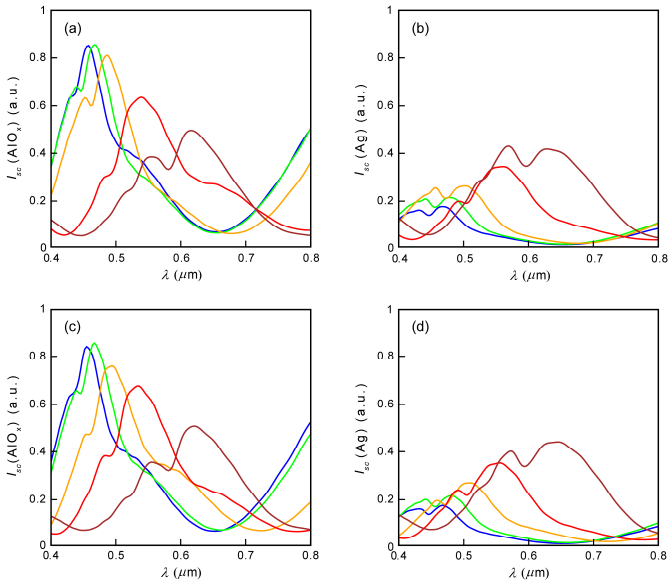

Fig. 11. Scattering intensity spectra from $|J_x|$ on top surface of aluminum oxide, $I_{SC}(\mathrm{AlO_x})$, and silver rod, $I_{SC}(\mathrm{Ag})$, in *x*-polarized, (a) and (b), and *y*-polarized excitation scheme, (c) and (d), for five different inter-nanorod gaps: 5 (brown lines), 10 (red lines), 15 (orange lines), 20 (green lines), 25 nm (blue lines).

For the SERS substrates based on the Ag nanorod arrays [2], enhanced localized electric field is induced at the gaps between adjacent Ag nanorods, as shown in this study. The Raman scattering process of the molecules residing at these uniformly distributed "hot spots" is therefore greatly enhanced. On the basis of the conclusion reached from this study, the surface electric field are not directly responsible for the observed far-field scattering spectrum

#110633 - $15.00 USD Received 27 Apr 2009; revised 7 Jul 2009; accepted 13 Jul 2009; published 31 Jul 2009

and the electric field located at these hot spots is mainly evanescent in nature [33], as demonstrated in Fig. 12. On the other hand, the fact that the surface magnetic field is responsible for the main characteristics of the far-field scattering spectrum allows us to suggest an alternative scenario of the physical processes involved in SERS based on these Ag nanorod arrays. The incident electromagnetic wave first interacts with the Ag nanorod array to create localized enhanced electric field at specific resonant wavelength. The molecules adsorbed on the top surface of the array then undergo the Raman scattering process with the localized electric field on the top surface, inducing emitting dipoles at Raman-shifted wavelengths that are not very far way from the wavelength of the incident light wave. The produced localized electric field by these emitting dipoles presumably has a very similar or even identical character as the one induced by the incident wave, assuming that the top surface is uniformly covered by the molecules. The concurrent magnetic field at the Raman-shifted wavelength on the top surface thus behaves similarly as the calculated surface magnetic field presented in this study. The scattering field in far zone at the Raman-shifted wavelength then carries the characteristic information of this surface magnetic field, owing to its propagating nature. In other words, the Ag nanorod array acts as the mediator between the Raman-induced localized electric field that is mainly evanescent in nature and the propagating surface magnetic field that is responsible for the far-field observation. The conclusion above is also reached in the *y*-polarized excitation scheme, as shown in Figs. 11(c) and (d). The verification of this suggested view certainly needs more in-depth experimental and theoretical studies. In particular, a comprehensive electrodynamic simulation of the whole Raman scattering process can open a unique opportunity to disclose the role of the nano-plasmonic structures in SERS.

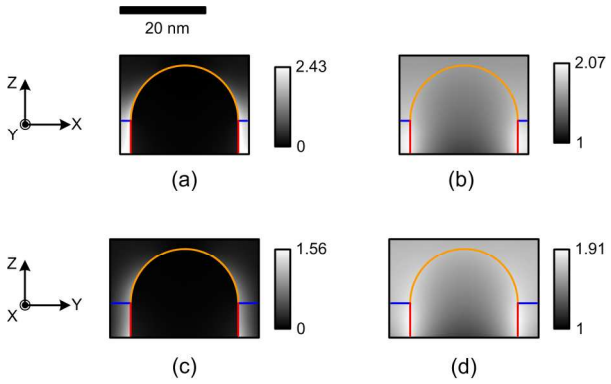

Fig. 12. Cross-sectional views of (a) electric and (b) magnetic fields at resonance of Ag nanorod array with W = 5 nm in *x*-polarized excitation scheme and corresponding ones of (c) electric and (d) magnetic fields in *y*-polarized excitation scheme. Orange lines represent vacuum-Ag interface; blue lines represent vacuum-AlO_x interface; red lines represent Ag-AlO_x interface.

4. Conclusions

We have successfully constructed a numerical procedure to calculate far-field scattering spectra of Ag nanorod arrays with different inter-nanorod gaps, which are in good agreement with experiment observation. The good agreement is realized with the following two efforts. First, an excellent fit to the dispersive material property of silver has been achieved with the Drude-Lorentz model. Second, this model has been implemented in a three-dimensional electrodynamic numerical scheme based on PSTD method, demonstrating an extreme small error in comparison with Mie theory. With this high precision calculation effort, we shows that the surface magnetic field of the Ag nanorod arrays is responsible for the main scattering characteristics in far field, while the surface electric field, although exhibiting localized

#110633 - $15.00 USD Received 27 Apr 2009; revised 7 Jul 2009; accepted 13 Jul 2009; published 31 Jul 2009

enhanced distribution ("hot spots"), plays a minor role. This anomalous origin of the far-field scattering has been found to be emanated from the fact that the surface electric field has a more evanescent-wave character than the surface magnetic field does, which has been mostly overlooked. The illustration of the respective roles of surface electric and magnetic fields provides a brand new scenario in designing highly efficient SERS substrates: Both the creation of enhanced electric field as well as the efficient transfer of the Raman-shifted light field to the far zone are important.

Appendix

Two optimization algorithms were adopted to retrieve the parameters in the curve-fitting action of Eq. (1) on the experimental dielectric function of sliver [18]. Firstly, an objective function is defined as

$$\Psi = \sum_j \left(\left\{ \mathrm{Re}\left[\varepsilon_{\exp}(\omega_j) - \varepsilon_{\mathrm{DL}}(\omega_j) \right] \right\}^2 + \left\{ \mathrm{Im}\left[\varepsilon_{\exp}(\omega_j) - \varepsilon_{\mathrm{DL}}(\omega_j) \right] \right\}^2 \right), \tag{A1}$$

where $\varepsilon_{\exp}$ and $\varepsilon_{\mathrm{DL}}$ are experimental data and the values calculated with the guessed parameters based on Eq. (1), respectively. The ω_j's are the discrete frequencies in the spectral range of interest (from 0.2 to 1 μm). The procedure was started by minimizing Ψ according to the genetic algorithm that has a good property of being insensitive to the initial guessed values. As the final values obtained with this algorithm seldom give the best result, nonlinear least square method was then utilized to further minimize Ψ. These two algorithms were then employed iteratively until good results were obtained. In the optimizing process, the least amount of Lorentz terms was used while maintaining minimum error. This approach was followed merely based on the law of parsimony. The extracted values of these parameters are listed as follows: ε_∞ = 3.7, ω_p = 8.40×10^{16} rad/sec, τ = 1.485×10^{-14} sec, f_1 = 0.065, ω_1 = 7.79×10^{15} rad/sec, Γ_1 = 3.71×10^{16} rad/sec, f_2 = 0.124, ω_2 = 4.25×10^{16} rad/sec, and Γ_2 = 5.73×10^{15} rad/sec. Figure A1 shows the comparison in dielectric function between the experimental data and the values obtained from the Drude-Lorentz model in the wavelength range from 0.2 to 1.0 μm. Notice that the relative differences in both real and imaginary parts, defined as

$$\mathrm{Re}[\Delta\varepsilon] = \mathrm{Re}\left[\varepsilon_{\mathrm{DL}} - \varepsilon_{\exp}\right] \Big/ \mathrm{Re}\left[\varepsilon_{\exp}\right] \quad \text{and} \quad \mathrm{Im}[\Delta\varepsilon] = \mathrm{Im}\left[\varepsilon_{\mathrm{DL}} - \varepsilon_{\exp}\right] \Big/ \mathrm{Im}\left[\varepsilon_{\exp}\right],$$

are within $\pm 5\%$ and $\pm 25\%$, respectively, from 0.4 to 0.8 μm.

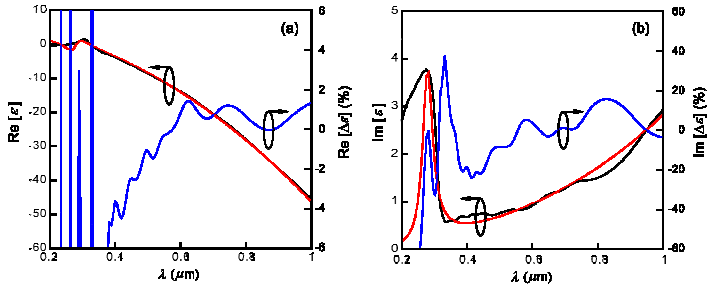

Fig. A1. Real (a) and imaginary (b) parts of relative permittivity, ε, of silver from 0.2 to 1.0 μm. Black lines represent experimental data, red lines represent the best-fit curve based on Drude-Lorentz model, and blue lines represent relative differences in percentage between them.

#110633 - $15.00 USD Received 27 Apr 2009; revised 7 Jul 2009; accepted 13 Jul 2009; published 31 Jul 2009

Acknowledgements

The authors thank the financial support by National Science Council (93-2811-M-001-090 and 96-2120-M-001-002) and Academia Sinica of Taiwan.

#110633 - $15.00 USD Received 27 Apr 2009; revised 7 Jul 2009; accepted 13 Jul 2009; published 31 Jul 2009